

# GAS SEGREGATION IN DIKES AND SILLS

Thierry Menand<sup>1</sup>, Jeremy C. Phillips

*Department of Earth Sciences, Centre for Environmental and Geophysical Flows,*

*University of Bristol, Bristol, UK*

10 January 2006

---

## Abstract

Many basaltic volcanoes emit a substantial amount of gas over long periods of time while erupting relatively little degassed lava, implying that gas segregation must have occurred in the magmatic system. The geometry and degree of connectivity of the plumbing system of a volcano control the movement of magma in that system and could therefore provide an important control on gas segregation in basaltic magmas. We investigate gas segregation by means of analogue experiments in a simple geometry consisting of a vertical conduit connected to a horizontal intrusion. Degassing is simulated by electrolysis, producing micrometric bubbles in viscous mixtures of water and golden syrup. The presence of exsolved bubbles induces a buoyancy-driven exchange flow between the conduit and the intrusion that leads to gas segregation. Bubbles segregate from the fluid by rising and accumulating as a foam at the top of the intrusion, coupled with the accumulation of denser degassed fluid at the base of the intrusion. Steady-state influx of bubbly fluid from the conduit into the intrusion is balanced by outward flux of lighter foam and denser degassed fluid. The length and time scales of this gas segregation are controlled by the rise of bubbles in the horizontal intrusion. Comparison of the gas segregation time scale with that of the cooling and solidification of the intrusion suggests that segregation is more efficient in sills than in horizontally-propagating dikes, and that this process could be efficient in intermediate as well as basaltic magmas. Our investigation shows that non-vertical elements of the plumbing systems act as strong gas segregators. Gas segregation also has implications for the generation of gas-rich and gas-poor magmas at persistently active basaltic volcanoes. For low magma supply rates, very efficient gas segregation is expected, which

---

<sup>1</sup>Corresponding author.

*Email addresses:* **T.Menand@bristol.ac.uk** (Thierry Menand),  
**J.C.Phillips@bristol.ac.uk** (Jeremy C. Phillips).

induces episodic degassing activity that erupts relatively gas-poor magmas. For higher magma supply rates, gas segregation is expected to be less effective, which leads to stronger explosions that erupt gas-rich as well as gas-poor magmas. These general physical principles can be applied to Stromboli volcano and are shown to be consistent with independent field data. Gas segregation at Stromboli is thought likely to occur in a shallow reservoir of sill-like geometry at 3.5 km depth with exsolved gas bubbles 0.1–1 mm in diameter. Transition between eruptions of gas-poor, high crystallinity magmas and violent explosions that erupt gas-rich, low crystallinity magmas are calculated to occur at a critical magma supply rate of  $0.1\text{--}1\text{ m}^3\text{ s}^{-1}$ .

## 1 Introduction

Magma degassing provides a fundamental control on the eruptive style of volcanoes. The activity of Kilauea, Hawaii, is characterized by short-lived, intense fire-fountaining and longer-lived gentle effusion of lava. In contrast, explosive activity such as the May 18<sup>th</sup> 1980 eruption of Mt. St. Helens is characterized by intense degassing in the volcanic conduit, leading to explosive fragmentation of silicic magma to form a Plinian eruption column and pyroclastic density currents. Although the duration and cyclicity of these two eruption styles are different, the initial dissolved gas content does not vary significantly between either style. Basaltic magmas typically contain 1–3 weight percent volatiles, although dissolved water contents as high as 6 weight percent have been measured in arc basalts (Sisson and Lane, 1993), whereas silicic magmas contain 4–6 weight percent volatiles (e.g., Wallace, 2001). Petrological, theoretical, and analog experimental studies suggest that the rate of degassing, and not the absolute volatile abundance, is of primary importance in controlling eruptive style (Sparks et al., 1994; Sparks, 2003). Processes that may affect the rate of degassing include ascent rate and nucleation. Degassing rate can also be strongly influenced by processes of gas segregation within the sub-surface magma.

Many basaltic volcanoes emit a substantial amount of gas while erupting relatively little, if any, degassed lava. Examples include Kilauea in Hawaii (Francis et al., 1993), Mount Etna (Allard, 1997) and Stromboli in Italy (Francis et al., 1993), Erta'Ale in Ethiopia (Le Guern et al., 1979), Nyiaragongo in Zaire (Le Guern, 1987), Masaya in Nicaragua (Stoiber et al., 1986) and Mount Erebus in Antarctica (Kyle et al., 1990). These volcanoes have been persistently degassing for years to millennia, which requires a physical separation of volatiles from the magma that must remain efficient over very long periods of time. Mass balance requires that large amounts of magma must be processed during gas segregation. This would imply growth of the volcanic plumbing system whereby influx of new, gas-bearing magma is stored at shallow depth where it degases. Alternatively, long-lived degassing can be achieved by a recirculation of magma between shallow parts of a volcanic plumbing system, where over-saturated volatiles can be extracted, and deeper parts of the system where degassed magma can be recycled. Regardless of the precise mechanism, gas segregation must occur so that exsolved volatiles are physically

decoupled and separated from the melt.

The main control on gas segregation is that the lower viscosity of mafic magmas allows the development of bubbly suspensions from which bubbles can escape more rapidly than from more viscous silicic melts (Vergnolle and Jaupart, 1990; Phillips and Woods, 2001). The process of gas segregation, however, does not simply result from gas bubbles rising more rapidly than the magma on ascent; even in very low viscosity basalts ( $\sim 1 \text{ Pa s}$ ) with typical ascent speeds on the order of  $0.1\text{--}1 \text{ m s}^{-1}$ , centimetric-scale bubbles are required for bubble rise speeds to exceed magma ascent speeds. In explosive basaltic eruptions, larger bubbles ( $> 1 \text{ cm}$ ) are observed in scoriae associated with fragmented flow in conduits where gas velocities exceed typical rise velocities. However, this centimetric scale bubble size is at least one order-of-magnitude larger than typical bubble diameters in basaltic lavas, intrusions, and scoriae (Sarda and Graham, 1990; Cashman and Mangan, 1994; and Sparks, 2003), suggesting that alternative mechanisms of gas segregation must be considered.

Rates of degassing in excess of those due to independent ascent of equilibrium-sized bubbles include bubble coalescence (Sparks, 2003), convection processes in conduits (Stevenson and Blake, 1998) and foam development in reservoirs (Jaupart and Vergnolle, 1989). A simple plumbing system with a single vertical conduit connected to a single deeper reservoir is usually assumed in process models. Volcanic plumbing systems, however, often involve a complex geometry of interconnected sub-units, from vertical conduits to horizontal dikes and sills and other sub-reservoirs of less well-defined geometry. For example, flank eruptions are usually fed by dikes propagating laterally from a summit conduit (Woods and Cardoso, 1997; Acocella and Neri, 2003), although such eruptions can involve a more complex degree of connectivity (Acocella and Neri, 2003; Andronico et al., 2005). Seismic studies of Kilauea volcano, Hawaii, suggest a three dimensional, interconnected plumbing system (Ryan et al., 1981; Ryan, 1988) with a complex plexus of sills and dikes beneath Halemaumau (Dawson et al., 2004). Evidence for complex plumbing systems also is apparent from geochemical studies, which suggest multistage magma ascent and degassing during the volcanic activity at, for example, Mt. St. Helens in 1980 (Berlo et al., 2004).

The geometry and degree of connectivity of the plumbing system could provide an important control on magma movement in the system and thus on gas segregation processes in basaltic magmas. Here we investigate 1) how the geometry and connectivity of the plumbing system affect the circulation of magma and 2) how this circulation impacts gas segregation. We restrict our investigation to the geometry of a vertical conduit connected to a horizontal magma body. This simple geometry enables the identification of the key physical principles that govern gas segregation in more complex magmatic plumbing systems. In section 2 we describe laboratory analogue experiments investigating bubble segregation in idealized geometry, and in section 3 we develop mathematical models for transient and steady-state flow driven by gas segregation processes. In section 4 we discuss the implications and limitations of our work in detail, before concluding in section 5.

## **2. Analog experiments**

### *2.1 Setup and Calibration*

We have carried out a series of analog laboratory experiments to investigate gas segregation in a simple geometry consisting of two interconnected glass tubes that simulated a vertical conduit connected to a horizontal intrusion with a closed end. Both ends of the vertical glass tube are connected to a peristaltic pump to form a recirculating flow loop (Fig.1). The internal diameter of the vertical tube was 4 cm, whereas the length and the diameter of the horizontal side arm were varied.

The solutions used as a magma analogue were various mixtures of golden syrup, water, and Sodium Chloride (NaCl). Density,  $\rho_l$ , and viscosity,  $\mu_l$ , of these Newtonian solutions were varied by changing the relative amount of water and golden syrup. Density was measured by weighing a known volume, and the viscosity was measured using a Haake RV20 viscometer. Properties of the experimental mixtures are summarised in Table 1.

Small bubbles were produced by electrolysis (Fig. 1) of the viscous NaCl solution to simulate magma degassing by cooling and crystallisation (Cardoso and Woods, 1996; Phillips and

Woods, 2002). An electrolysis cell was set up in the vertical tube using a 20 mesh nickel gauze with wire diameter 180  $\mu\text{m}$  as the cathode and a platinum wire as the anode. The nickel gauze was positioned across the vertical tube below its junction with the horizontal side arm, and the platinum wire was situated 5 cm above. A 35 V power supply drove the electrolysis cell. Bubble size distributions were measured by pressing samples of the mixtures between two glass plates 0.5 mm apart. Bubbles rose and collected on the upper glass plate, and a digital image was taken through a microscope at 4 $\times$  magnification. A typical image contained approximately 150 bubbles. The mean bubble diameter,  $d$ , was measured for different golden syrup:water:NaCl mass ratios, and one standard deviation was used as a measure of the bubble size distributions. Mean bubble diameters of  $25 \pm 10 \mu\text{m}$  and  $35 \pm 21 \mu\text{m}$  were measured for mixture mass ratios of 45:45:10 and 60:30:10, respectively. These values were used together with the solution viscosity to calculate the bubble rise speed using Stokes law and showed that bubbles rose at an average speed of  $0.06 \text{ mm s}^{-1}$  and  $0.03 \text{ mm s}^{-1}$  in the 45:45:10 and 60:30:10 mixtures, respectively. The low viscosity of 30:60:10 mixtures meant that most of the bubbles escaped during the sample preparation, preventing any reliable measurement.

The gas flux produced by electrolysis was calibrated by installing the anode and cathode in the vertical tube without a side arm, but connected to a 1 mm diameter capillary tube at the upper end. The tube was filled with a golden syrup:water:NaCl mixture. The fluid was not circulated by the pump during the calibration measurements. Gas produced by electrolysis drove a liquid film up this tube, and recording of its successive positions enabled the gas flux to be estimated. As shown in Fig. 2, these experimental measurements enable the gas production rate  $Q_g$  to be related to electric current intensity  $I$  by the linear relationship

$$Q_g = (1.43 \pm 0.03) \times 10^{-7} \times I \text{ m}^3 \text{ s}^{-1}, \text{ where } I \text{ is expressed in Ampere.}$$

The volumetric gas fraction,  $c$ , produced by electrolysis was calibrated by weighing known volumes of bubble-free liquid and bubbly fluid. The ratio of the measured mass of bubbly fluid,  $m_b$ , to that of the bubble-free liquid,  $m_o$ , is the volumetric fraction of liquid so that

$c = 1 - m_b / m_o$ . This procedure was repeated for different electric current intensities. Electric current intensity in the range 0–0.5 Ampere gives gas fractions in the range 0–5 volume percent. These measurements, however, lead to high systematic uncertainties of typically 1–2 volume percent. It was therefore decided to use the gas fraction as a fitting parameter when comparing model and experiments, provided the fitting values are concordant with the gas production rates. Because gas production rate increases linearly with electric current intensity (Fig. 2) and gas fraction is proportional to gas production rate, the gas fraction also must increase linearly with electric current intensity.

At the start of an experiment, the apparatus was filled with golden syrup:water:NaCl mixture and all gas bubbles introduced by the filling process were removed. The experiment was initiated by setting the peristaltic pump to a desired flow rate. The electrolysis cell was then switched on, and the desired gas flux was set independently of the liquid flux. Experimental duration was measured from the time that the electrolysis cell was switched on, and the position of the interface between the bubbly liquid, the foam layer, and bubble-free liquid was measured as the experiment proceeded.

## *2.2 Observations*

We have investigated a range of liquid and gas flow rates from the case of no fluid flow (i.e., bubbles rose through and separated from the liquid in the vertical tube) to that of a fluid flow rate 80 times larger than the gas flux (i.e., bubbles were carried by and rose at the same speed as the liquid).

Irrespective of the flow rate in the vertical tube, the same fluid-flow processes were observed. At the beginning of the experiments, the electrolysis creates bubbles that rise up the vertical conduit. These bubbles decrease the bulk density of the mixture, which creates a density difference between the bubbly fluid rising in the vertical conduit and the bubble-free fluid originally at rest in the horizontal side arm. In turn, this density difference drives an exchange flow between the two tubes (Fig. 3A). The time-scale associated with this exchange is long

enough that bubbles in the horizontal side arm have time to rise, segregate from the fluid, and accumulate at its top. This segregation is coupled with the accumulation of degassed fluid at the base of the side arm (Fig. 3B). Ultimately, a steady state is reached whereby the influx of bubbly fluid into the side arm is balanced by the outward flux of lighter foam and denser degassed fluid, which are respectively reinjected up the conduit toward the surface, and recycled at depth in the vertical section (Fig. 3C). The structure of the fluid stratification in the side arm is then fixed, with the thickness of both the foam and the layer of degassed fluid remaining constant.

### 3. Model

#### 3.1 Transient exchange flow

Before modeling the gas segregation in the side arm, let us focus on the buoyancy-driven exchange flow set up between the rising bubbly fluid with density  $\rho_b$ , and the initially bubble-free fluid with density  $\rho_l$  in the horizontal arm of thickness  $D$ . Modeling this transient exchange flow will allow us to determine how the length,  $L$ , of the intruding bubbly current evolves with time, and therefore the areal extent of the bubbly source for gas segregation. Fig. 4 shows a schematic diagram of the transient flow.

We treat the inflowing bubbly flow as a viscous gravity current. After an initial adjustment, we assume that the pressure distribution in the bubbly current becomes hydrostatic because of negligible vertical accelerations. Excess pressure driving the exchange flow comes from the density difference between the bubbly fluid and the bubble-free fluid,  $\Delta\rho = \rho_l - \rho_b$ , and is balanced by viscous dissipation. Density of the bubbly fluid is a function of the liquid density, the gas bubble density  $\rho_g$ , and the gas fraction  $c$ :  $\rho_b = c\rho_g + (1 - c)\rho_l$ . Because  $\rho_l \gg \rho_g$ , the density difference that drives the flow simplifies to

$$\Delta\rho = c\rho_l. \quad (1)$$

The viscosity of the bubbly fluid,  $\mu_b$ , can be estimated from the viscosity of the bubble-free fluid,  $\mu_l$ , and the volumetric gas fraction,  $c$ , in the current. Experimental gas fractions were



typically less than 0.1, permitting the viscosity of the bubbly fluid to be approximated as (Wallis, 1969; Jaupart and Vergnolle, 1989)

$$\mu_b = \mu_l(1 + c). \quad (2)$$

For these low gas fractions, viscosities of the bubbly current and the bubble-free fluid only differ by a few percent. As a result, the advance of the current is resisted by viscous dissipation occurring within as well as around the bubbly current (Huppert, 1982). The exact mathematical treatment of the problem is thus complex, but we can use arguments based on dimensional analysis to find how the current length varies as a function of the other relevant variables.

The bubbly current length,  $L$ , depends on the side arm diameter,  $D$ ; the gravitational pressure gradient,  $\Delta\rho gD / L$ , where  $g$  is the gravitational acceleration; the viscosity of the bubbly fluid,  $\mu_b$ ; bubble-free fluid,  $\mu_l$ ; and time,  $t$ :

$$L = L\left(\frac{\Delta\rho gD}{L}, D, \mu_b, \mu_l, t\right). \quad (3)$$

Dimensional analysis yields the following three dimensionless groups

$$\Pi_1 = \frac{L}{D}, \quad \Pi_2 = \frac{\mu_l}{\mu_b}, \quad \Pi_3 = \frac{\Delta\rho gDt}{\mu_b}, \quad (4)$$

such that  $\Pi_1 = \Phi(\Pi_2, \Pi_3)$  where  $\Phi$  is an unknown function that needs to be defined (Barenblatt, 1996). Thus, the length of the current can be expressed as

$$L = D\Phi\left(\frac{\mu_l}{\mu_b}, \frac{\Delta\rho gDt}{\mu_b}\right). \quad (5)$$

We do not know the form of function  $\Phi$  but can use the following physical argument to estimate it. The fluid current is driven by the gravitational pressure gradient; the current would not exist if there were no density difference between the bubbly and bubble-free fluids. This density difference depends on the volumetric gas fraction  $c$  (equation 1), thus,  $L$  must be directly

proportional to  $\Delta\rho$ , and therefore proportional to the dimensionless group  $\Delta\rho gDt / \mu_b$ . We now make the assumption that the dependence of  $L$  on the density difference follows a power law, which is a common assumption when using dimensional analysis. That is, the dimensionless group  $\Delta\rho gDt / \mu_b$  can be raised to some power  $\alpha$ , from which we get the following expression for the current length:

$$L = D \left( \frac{\Delta\rho gDt}{\mu_b} \right)^\alpha F \left( \frac{\mu_l}{\mu_b} \right). \quad (6)$$

The time dependence  $t^\alpha$  of the current length does not depend on the viscosity ratio  $\mu_l / \mu_b$  (equations 5 and 6). Therefore, this time dependence should remain the same whatever the viscosity ratio is, and we can choose the viscosity ratio to simplify the problem and determine  $\alpha$ . In the particular case of a gravity current that is much more viscous than the surrounding fluid, advance of the current is resisted mainly by internal viscous dissipation (Huppert, 1982). Thus, the buoyancy-viscous balance that governs the current flow is

$$\frac{\Delta\rho g D}{L} \sim \mu_b \frac{L}{D^2 t} \quad (7)$$

and the length of the current increases with time as  $L \sim (\Delta\rho g D^3 t / \mu_b)^{\frac{1}{2}}$ . This time dependence of  $L$  is independent of the viscosity ratio, so we expect  $L$  to increase with time similarly in the general case:

$$L(t) = \left( \frac{\Delta\rho g D^3 t}{\mu_b} \right)^{\frac{1}{2}} F \left( \frac{\mu_l}{\mu_b} \right) \quad (8)$$

where  $F$  is an unknown function of the viscosity ratio  $\mu_l / \mu_b$ .

We use the experiments to test the time dependence of the bubbly current given by equation (8).

There is a maximum distance,  $L_{\max}$ , that the current can travel, which corresponds to the point where all bubbles have risen to the top of the side arm. Because of low bubble concentrations, bubble interactions can be neglected, and bubbles rise according to Stokes law with constant velocity,  $v_b = (\Delta\rho_g g d^2) / (12\mu_l)$ , where  $\Delta\rho_g$  is the difference between the density of the pure liquid and the gas bubble,  $\Delta\rho_g = \rho_l - \rho_g$ , and  $d$  is the bubble diameter [the numerical constant 12 at the denominator differs from the usual constant 18 because of the constant stress condition at the bubble surface between the inner gas and the outer liquid, whereas the constant 18 should arise in the case of a rigid sphere on which surface a no slip condition applies (Batchelor, 1967)]. Because  $\rho_l \gg \rho_g$ , the density difference can be approximated by

$\Delta\rho_g = \rho_l$ , and bubbles rise at speed

$$v_b = (\rho_l g d^2) / (12\mu_l). \quad (9)$$

The maximum distance that bubbles can rise is the diameter,  $D$ , of the side arm, so the maximum time that bubbles take to reach the top of the side arm is

$T_b = D / v_b = 12\mu_l D / (\rho_l g d^2)$ . Therefore, the maximum current length is:

$$L_{\max} = L(T_b) = \left[ \frac{12\mu_l \Delta\rho D^4}{\mu_b \rho_l d^2} \right]^{\frac{1}{2}} F\left(\frac{\mu_l}{\mu_b}\right). \quad (10)$$

Substituting equations (1) for  $\Delta\rho$  and (2) for  $\mu_b$ , the maximum current length becomes

$$L_{\max} = \frac{D^2}{d} \left( \frac{12c}{1+c} \right)^{\frac{1}{2}} F\left(\frac{\mu_l}{\mu_b}\right). \quad (11)$$

Evolution of the bubbly current length in the experiments was measured by recording the successive positions of the tip until advance ceased. For each experiment, the length of the current has been non-dimensionalised on the maximum length,  $L_{\max}$ , attained by the current, allowing

comparison over a range of conditions. This approach enables us to eliminate the unknown function  $F$ . Fig. 5 shows the experimental dimensionless current length as a function of the theoretical dimensionless length  $L^* = L(t) / L_{\max} = \left[ \rho_l g d^2 t / (12 \mu_l D) \right]^{\frac{1}{2}}$ . After an initial adjustment phase, the data collapse onto the theoretical relationship up to the point where the current has reached its maximum length. Beyond this point,  $L^*$  remains equal to unity as the bubbly current has ceased to propagate. In the adjustment phase, data are quite scattered, and in some experiments the measured length needs to reach almost 60% of the theoretical maximum length before the measured length follows the theoretical relationship. However, the adjustment phase is shorter for most experiments. Close examination of the data reveals that the initial mismatch appears proportional to the velocity scale in the vertical conduit (either the average fluid velocity imposed by the pump or the bubble rise speed when no fluid was circulated by the pump). This suggests that the initial spread of the bubbly gravity current is controlled, in some way, by the vertical movement of bubbly fluid up the conduit. Fig. 5 shows, however, that ultimately the bubbly current is controlled by the segregation of the bubbles from the fluid as they rise and accumulate at the top of the horizontal arm; the advance of the bubbly gravity current is then described by  $L^*$ .

### 3.2 Gas segregation and foam development

We now consider the bubble segregation that occurs in the bubbly current. This problem is similar to that investigated by Jaupart and Vergnolle (1989) and we shall base our analysis on their model.

We approximate the foam as a long and thin viscous gravity current, in which the vertical acceleration is negligible and pressure is hydrostatic (Fig. 6). Thus, the flow is driven by the horizontal gradient of the hydrostatic pressure and resisted by the viscous stresses. The foam, however, is much more viscous than the underlying fluid because of a high gas content,  $\varepsilon$ , that is approximately 70% by volume. Foam viscosity,  $\mu_f$ , is well approximated by the relationship

(Jaupart and Vergnolle, 1989)

$$\mu_f = \mu_l (1 - \varepsilon)^{\frac{-5}{2}}. \quad (12)$$

Using this expression, a foam with 70 volume percent bubbles is approximately 20 times more viscous than the underlying fluid. Therefore, the main viscous dissipation that resists the flow occurs within the foam and the shear stress at the interface between the foam and the bubbly fluid can be neglected (Huppert, 1982). Consequently, the problem allows analytical treatment.

The horizontal flow is governed by the momentum equation

$$\Delta\rho_f g \frac{\partial h}{\partial x} = \mu_f \frac{\partial^2 u}{\partial z^2}, \quad (13)$$

where  $x$  is the horizontal distance from the entrance of the side arm and  $z$  the vertical distance from its top.  $\Delta\rho_f$  is the density difference between the bubbly fluid ( $\rho_b = (1 - c)\rho_l$  because  $\rho_l \gg \rho_g$ ) and the foam ( $\rho_f = (1 - \varepsilon)\rho_l$ ), such that  $\Delta\rho_f = (\varepsilon - c)\rho_l$ . Integrating the momentum equation (13) with the two boundary conditions of (i) no slip at the top of the side arm,  $u(z = 0) = 0$ , and (ii) no shear stress at the interface,  $\frac{\partial u}{\partial z} = 0$  for  $z = h$ , gives the foam

velocity,  $u$ , as

$$u = \frac{\Delta\rho_f g z}{2\mu_f} (z - 2h) \frac{\partial h}{\partial x}. \quad (14)$$

Mass conservation for gas in the foam layer can be expressed as

$$\frac{\partial h}{\partial t} = q - \frac{\partial}{\partial x} \int_0^h u dz. \quad (15)$$

The left hand term represents the vertical growth of the foam thickness. It is balanced on the right by two terms: the gas flux per unit area,  $q$ , that is supplied by the underlying bubbly current, and

a second term representing the outward flux of foam per unit area into the vertical conduit that represents the lateral extent of the foam, which is controlled by the foam velocity  $u$ . In the bubbly current, the rise of bubbles is characterised by the rise speed,  $v_b$ , (9) so the vertical gas flux per unit area that feeds the foam is  $q = cv_b / \varepsilon$ . Using the foam velocity (14) to integrate the foam mass balance (15), we get

$$\frac{\partial h}{\partial t} = q + \frac{\Delta\rho_f g}{12\mu_f} \frac{\partial^2 h^4}{\partial x^2}. \quad (16)$$

This equation is non-dimensionalised using the scales  $x = Lx'$ , where  $L$  is the length of the underlying bubbly current,  $h = Hh'$ , and  $t = Ht'/q$ , with  $H = \left[ (12\mu_f q L^2) / (\Delta\rho_f g) \right]^{\frac{1}{4}}$  and

where the primes denote dimensionless variables:

$$\frac{\partial h'}{\partial t'} = 1 + \frac{\partial^2 h'^4}{\partial x'^2}. \quad (17)$$

We seek the steady-state shape of the foam,  $\frac{\partial h'}{\partial t'} = 0$ . Integrating this equation twice with the

boundary conditions of (i) zero foam thickness at the entrance of the side arm,  $h'(x' = 0) = 0$ ,

and (ii) no lateral foam flux at the end of the side arm,  $\frac{\partial h'}{\partial x'} = 0$  for  $x' = 1$ , gives

$$h'(x') = \left( x' - \frac{x'^2}{2} \right)^{\frac{1}{4}}. \quad (18)$$

Therefore, expressed in dimensional variables, the height of the foam,  $h$ , can be written as the product of a characteristic height,  $H$ , and a shape function,  $f(x)$ :

$$h(x) = Hf(x), \quad (19)$$

where

$$H = \left[ \frac{12\mu_f q L^2}{\Delta\rho_f g} \right]^{\frac{1}{4}}, \quad (20)$$

and

$$f(x) = \left( \frac{x}{L} - \frac{x^2}{4L^2} \right)^{\frac{1}{4}}. \quad (21)$$

From equation (20), the characteristic foam height can be simplified further by recalling that  $\Delta\rho_f = (\varepsilon - c)\rho_l$ ,  $q = cv_b / \varepsilon$ , and by using equations (9) for  $v_b$  and (12) for  $\mu_f$ :

$$H = \left[ \frac{cd^2 L^2}{\varepsilon(1 - \varepsilon)^{\frac{5}{2}} (\varepsilon - c)} \right]^{\frac{1}{4}}. \quad (22)$$

This two-dimensional analysis does not account for the cap-like geometry of the foam in the cylindrical side arm used in the experiments; the foam is assumed to have a constant thickness over its entire width, perpendicular to the direction of flow (i.e., Fig. 6). Consequently, at a given position along the side arm, for a given foam flux per area perpendicular to the flow, the predicted foam height is underestimated by the theory (i.e., dotted rectangle in Fig. 7). Because the foam has in fact a cap-like cross section, it requires a greater height to accommodate the same flux (i.e., striped area in Fig. 7). To compare the model with the experiments, the theoretical height was increased so that it gives the same foam flux in both the theoretical model and the experiments (Fig. 7).

To calculate the foam height, we also need to know the foam gas fraction,  $\varepsilon$ . Stable foams typically contain approximately 70 volume percent of gas (Jaupart and Vergnolle, 1989). This value is likely to be a lower bound in our experiments, however, because the fine bubbles produced by electrolysis tend to coalesce and create centimetric to decimetric bubbles at the top of the foam. Observation indicates that the foam gas fraction in the experiments is therefore more likely to be in the range of  $\varepsilon = 0.7 - 0.9$ .

For each experiment, the steady-state foam thickness was measured from a digital photograph at different positions along the tube, with an uncertainty of  $\pm 1$  mm. The gas fraction,  $c$ , in the bubbly layer was used as a fitting parameter when comparing experimental and theoretical steady-state foam thicknesses (see section 2.1). The foam height is also very sensitive to the foam gas fraction,  $\varepsilon$ , because it is close to unity (equation 22). Fig. 8 shows the foam thickness measured along the side arm in three experiments that differ by their electrolysis electric current intensities, and hence gas fraction,  $c$ . In all three experiments, the theoretical thickness predicted by the model is shown for a foam gas fraction  $\varepsilon = 0.7$  and  $\varepsilon = 0.9$ . Our simple foam model is in good agreement with the data. Unrealistically high bubbly gas fractions, however, are required if the foam is assumed to contain 70 volume percent gas (Fig. 8B and 8C). More realistic values are obtained if instead the foam gas fraction is higher, in accord with the experimental observations.

We have implicitly assumed that the flow of rising fluid in the vertical conduit has no effect on the exchange flow and gas segregation that occur in the side arm. Fig. 9 shows that this assumption is indeed correct. Foam thickness was measured in three experiments that differ by their vertical conduit fluid flux,  $Q_l$ , only:  $Q_l = 0$ ,  $Q_l = 9Q_g$  and  $Q_l = 79Q_g$ , with

$Q_g = 2.9 \times 10^{-8} \text{ m}^3\text{s}^{-1}$  in all three experiments. Within the experimental errors, the foams that

developed in these three experiments have identical thicknesses even though the fluid flux varied over two orders of magnitude in the vertical conduit.



Finally, the lateral extent of the foam will be larger than the underlying bubbly current length,  $L_{\max}$ , if the side arm is longer than  $L_{\max}$ . In this case, as bubbles accumulate at the top of the side arm, the foam tip opposite the vertical conduit rests against a bubble-free fluid of higher density. The foam will therefore flow towards the closed end of the side arm until ultimately reaching a constant thickness. The steady-state foam thickness is then described by equations (19-21) between the entrance of the side arm and  $x = L_{\max}$ , and will have value  $h(x = L_{\max})$  away from the entrance.

#### 4. Implications and limitations

##### 4.1 Time scales

To apply this model of gas segregation to magma degassing, the time scale needs to be smaller than that of magma cooling and solidification. Two time scales arise in our model: a bubble time scale,  $T_b$  (for bubbles to rise over the thickness of the horizontal intrusion), and a foam time scale,  $T_f$  (to establish a steady-state foam). Cooling and solidification of magma occur over a time scale  $T_s$ .

Bubbles rise in the laminar regime according to Stokes law, so

$$T_b = \frac{12\mu_l D}{\rho_l g d^2}. \quad (23)$$

$T_f$  is obtained by dividing the characteristic foam thickness  $H$  (equation 22) by the foam velocity scale  $q$ ,

$$T_f = \frac{12\mu_l L^{\frac{1}{2}}}{\rho_l g d^{\frac{3}{2}}} \left[ \frac{\varepsilon^3}{c^3 (1-\varepsilon)^{\frac{5}{2}} (\varepsilon - c)} \right]^{\frac{1}{4}}. \quad (24)$$

Throughout our calculations we assume a foam gas fraction  $\varepsilon = 0.7$ . Although foams in our

experiments have higher gas fraction, a value of 0.7 is a generally accepted value for generic foams and thus seems a reasonable value for magmatic systems (Jaupart and Vergnole, 1989). The time needed to cool and solidify an intrusion of thickness,  $D$ , by conduction is

$$T_s = \frac{D^2}{16\kappa\lambda^2}. \quad (25)$$

Magma thermal diffusivity  $k = 5 \times 10^{-7} \text{ m}^2\text{s}^{-1}$  and the dimensionless constant  $\lambda$ , which depends on the temperature difference between the magma and surrounding rocks and is typically in the range 0.5–0.75 (Turcotte and Schubert, 1982). Throughout our calculations, we assume  $\lambda = 0.5$ .  $T_s$  is a lower estimate; if the intrusion were connected to an active conduit, the solidification time would be larger as any exchange flow would mean both mass and heat are exchanged, keeping the intrusion hotter than in the purely conductive scenario.

Fig. 10 shows the three time scales as a function of magma viscosity for sills with a thickness:length aspect ratio of 1:100. All three time scales increase with the intrusion size, but  $T_s$  is more sensitive to size than  $T_b$  and  $T_f$ . In consequence, efficient gas segregation in smaller sills would require magmas of relatively lower viscosity than in larger intrusions. The foam time scale decreases with increasing volumetric gas fraction,  $c$ , so gas segregation is favoured in magmas with higher volumetric gas fraction. The time scales also are strongly sensitive to the bubble size (Fig. 11). An order of magnitude change in bubble diameter affects  $T_b$  and  $T_f$  by two orders of magnitude (equations 23 and 24).

Using the exsolved gas fraction  $c = 0.01 - 0.1$  and bubbles 1 mm in diameter as reasonable values for shallow magmatic degassing, efficient gas segregation in a sill 10-m thick and 1-km long would require magmas of viscosity lower than  $10^3 - 10^4$  Pa s, whereas in a sill 100-m thick and 10-km long, gas segregation would remain efficient with magma viscosity as high as  $10^5$  Pa s. Recalling that  $T_s$  is a lower estimate for the solidification time, gas segregation by foam

formation in sills is a supportable process for intermediate as well as basaltic magmas.

We expect gas segregation to be more efficient in sills than in dikes. Dikes typically have a thickness:length aspect ratio of 1:1000 whereas the sill aspect ratio is usually 1:100, reducing  $T_s$  by a factor of 100. Bubble rise time also is substantially increased for a dike. Both effects reduce gas segregation efficiency. Our analysis, however, does not account for two processes that both would increase the solidification time scale. The first one is the advection of heat induced by any exchange flow between an active vertical conduit and a horizontal dike. The second is bubble convection, which has not been considered for any geometry (see section 4.4). Consequently, the solidification time scale would be longer and gas segregation could occur in dikes containing magmas of low viscosity.

#### *4.2 Implications for gas segregation*

Different eruptive scenarios can be envisaged depending on the values of supply rate,  $Q_s$ , exchange rate associated with gas segregation,  $Q_{ex}$ , foam layer return flow,  $Q_g$ , and degassed magma return flow,  $Q_D$  (Fig. 12). We infer from our experiments that gas segregation processes and rates in an intrusion will be independent of moderate changes in magma supply rate because the exchange of magma and gas between the conduit and the horizontal intrusion is predominantly driven by the gas segregation that occurs in the latter. Thus, the exchange rate does not depend on the magma supply rate. If magma supply rate is low and  $Q_{ex} > Q_s$ , then effective gas segregation can occur in the intrusion and can lead to episodic Strombolian eruptions of relatively gas-poor magma ( $Q_D$ ) driven by the rise of expanding foam packets and slugs up the conduit. If the magma supply rate is sufficiently large that it exceeds the exchange rate,  $Q_s > Q_{ex}$ , then there will be ineffective gas segregation suggestive of stronger explosions driven mainly by the deep supply in fresh magma and therefore erupting gas-rich ( $Q_s$ ) as well as gas-poor ( $Q_D$ ) magmas.

As illustrated in Fig. 12, the steady-state volumetric flux of bubbly fluid entering an intrusion,  $Q_{ex}$ , is balanced by an outward gas flux, or foam layer return flow,  $Q_g$ , and a degassed magma return rate,  $Q_D$ , so that  $Q_{ex} = Q_g + Q_D$ . A proportion,  $c$ , of  $Q_{ex}$  is made of exsolved gas,  $Q_g = cQ_{ex}$ . By mass balance,  $Q_D = (1 - c)Q_{ex}$ . The gas return flux is  $Q_g = Acv_b / \epsilon$ , where  $A$  is the interface area between the bubbly fluid and the foam in the intrusion. Assuming  $A$  is similar to the surface area of the intrusion,  $A \sim L^2$ , and using equation (9) for the bubble rise speed, it follows that

$$Q_{ex} = \frac{\rho_l g d^2 L^2}{12 \mu_l \epsilon}, \quad (26)$$

$$Q_D = \frac{(1 - c) \rho_l g d^2 L^2}{12 \mu_l \epsilon}, \quad (27)$$

$$Q_g = \frac{c \rho_l g d^2 L^2}{12 \mu_l \epsilon}. \quad (28)$$

These fluxes are shown in Fig. 13 as function of magma viscosity for two different bubble diameters,  $d = 0.1$  mm and  $d = 1$  mm.

We expect a transition between Strombolian activity when  $Q_s < Q_{ex}$ , and more explosive eruptions when  $Q_s > Q_{ex}$  to occur when both fluxes are comparable,

$$Q_s \sim Q_{ex} = \frac{\rho_l g d^2 L^2}{12 \mu_l \epsilon}. \quad (29)$$

As shown on Fig. 13, the transition to more explosive eruptions would require a much higher supply rate with low viscosity magmas than with more viscous magmas; low viscosity produces very effective gas segregation. Bubble size has also a strong effect and will increase with

decreasing pressure, which also increases  $Q_{ex}$ . Thus, we expect gas segregation processes to become more important at lower pressure (i.e., shallower depths).

#### 4.3 *Stromboli Volcano*

We can apply these general principles to degassing and eruption processes at Stromboli volcano, Italy. Stromboli has been experiencing continuous phases of activity for millenia (Allard et al., 1994). Persistent activity consists of mild explosions occurring every tens of minutes associated with a more quiescent, continuous open-conduit degassing from the summit craters, while extruding very little basalt. Between 1980 and 1993, the time-averaged gas mass flux has been estimated at  $6\text{--}12 \times 10^3$  tons per day ( $350\text{--}680 \text{ m}^3 \text{ s}^{-1}$ ). The associated flux of degassed magma,  $Q_D$ , estimated from measured  $\text{SO}_2$  flux, was  $0.3\text{--}0.6 \text{ m}^3 \text{ s}^{-1}$ , which is two orders of magnitude greater than the observed magma eruption rate of approximately  $2.5 \times 10^{-3} \text{ m}^3 \text{ s}^{-1}$  (Allard et al., 1994). This degassing is predominantly quiescent (Allard et al., 1994).

Normal Strombolian activity erupts highly porphyritic (HP) black scoria, lapilli, ash, and occasionally lava with approximately 50 volume percent crystals (Francalanci et al., 1999; Métrich et al., 2001). This normal activity is punctuated by more violent and paroxysmal eruptions that eject crystal-poor ( $< 5$  volume percent phenocrysts) and highly vesiculated pumices and scoriae that are referred to as low porphyritic (LP), in addition to crystal-rich, dense HP scoriae identical to the products of normal activity (Francalanci et al., 1999; Métrich et al., 2001). Petrological evidence reveals that LP products represent fresh, crystal-poor, gas-rich magma that feeds the plumbing system and HP products are the stored and differentiated form of the fresh magma (Francalanci et al., 1999).

Thermal and gas budget balances indicate that the plumbing system of Stromboli has been in steady state for millenia (Giberti et al., 1992; Allard et al., 1994; Harris and Stevenson, 1997).  $\text{CO}_2$ - and  $\text{H}_2\text{O}$ -rich magma is continuously supplied from a deep reservoir into the crystal-rich shallow plumbing system where it undergoes crystallization driven by decompression and volatile loss at low pressure (Métrich et al., 2001). Pressure estimates from fluid inclusions in restitic

quartzite nodules suggest a three stage plumbing system with (i) a deep reservoir at about 11 km depth ( $\approx 290$  MPa), (ii) a shallow reservoir at about 3.5 km depth ( $\approx 100$  MPa), and (iii) a near-surface reservoir (Vaggelli et al., 2003; Francalanci et al., 2004). The latter corresponds to the location of shallow explosive activity about 250 m below the surface (Chouet et al., 1997; Ripepe et al., 2001; Chouet et al., 2003), whereas the 3.5-km-deep reservoir is envisaged as the crystal-rich HP body ( $\rho_l = 2700 \text{ kg m}^{-3}$ ,  $\mu_l = 1.4 \times 10^4 \text{ Pa s}$ ) that is continuously renewed by deeper volatile-rich LP magma (2.4–2.8 weight percent  $\text{H}_2\text{O}$ ,  $\rho_l = 2500 \text{ kg m}^{-3}$ ,  $\mu_l = 15\text{--}20 \text{ Pa s}$ ) (Métrich et al., 2001). Brittle deformation of  $\text{CO}_2$ -rich fluid inclusions suggests rapid ascent of the gas-rich magma from a deep to a shallow reservoir, implying a high magma flow rate. Fast ascent and injection of gas-rich magma into the 3.5-km-deep reservoir has been proposed to cause the more violent explosions at Stromboli (Vaggelli et al., 2003).

We apply the general principles of gas segregation and generation of gas-rich and degassed magma identified in our experiments to these processes at Stromboli. The geometry of the shallow reservoir at 3.5 km is not well constrained, mainly because the seismicity is restricted to very shallow depths ( $< 1$  km) (Chouet et al., 2003), and there is poor knowledge of the internal structure of the volcano (Chouet et al., 1997). Nevertheless, 3.5 km corresponds approximately to the transition to crustal basement, where a lithological discontinuity is expected (Vaggelli et al., 2003), which is favorable to the formation of a sill-like reservoir. Analysis of Sr isotope ratios of scoria and lavas from Stromboli enabled Francalanci et al. (1999) to estimate the volume of this shallow reservoir at approximately  $0.3\text{--}0.04 \text{ km}^3$ . We calculate the reservoir dimensions assuming two bounding geometries: (i) a disk-like sill with a thickness:length aspect ratio of 1:100, whose volume would require an average thickness  $D = 25$  m and diameter  $L = 2.5$  km, and (ii) an equant body with diameter  $D = 500$  m. The true geometry of the Stromboli shallow reservoir is likely to lie in between these two end members.

Estimating *a priori* bubble sizes in the range 0.1–1 mm, which is reasonable for shallow basaltic systems (Sarda and Graham, 1990; Cashman and Mangan, 1994), time scales have been calculated for the sill-like geometry (Fig. 11) and the equant body (Fig. 14) using equations

23–35. Recalling that  $T_s$  is a lower estimate for the solidification time, Figs. 11 and 14 show that, regardless of the shallow chamber geometry, sufficient time is present for gas segregation to occur at Stromboli (gas-poor magma viscosity  $\sim 10^4$  Pa s) with bubble diameters in the range 0.1–1 mm. In comparison, Francalanci et al. (1999) estimated the average magma residence time in the shallow reservoir at  $\tau \sim 19 \pm 12$  years (i.e.,  $6 \pm 4 \times 10^8$  s). In our model, we assume that gas segregation occurs on a time scale shorter than the magma residence time. Although this is not a severe restriction for the sill-like geometry, because the residence time is comparable to the solidification time (Fig. 11), gas segregation in an equant body of gas-poor magma would only be possible with bubble diameters  $\sim 1$  mm or larger (Fig. 14).

The average magma residence time and volume estimated by Francalanci et al. (1999) for the shallow reservoir enable us to calculate an exchange flow rate of order

$Q_{ex} \sim V / \tau \sim 0.07 - 0.5 \text{ m}^3 \text{ s}^{-1}$ . This rate is in the range given by Giberti et al. (1992)

( $\sim 0.06 \text{ m}^3 \text{ s}^{-1}$  estimated from thermal and gas budget balances) and Allard et al. (1994)

( $0.3\text{--}0.6 \text{ m}^3 \text{ s}^{-1}$  estimated from measured  $\text{SO}_2$  flux). Assuming  $\rho_l = 2700 \text{ kg m}^{-3}$ ,

$\mu_l = 1.4 \times 10^4 \text{ Pa s}$ , and  $\varepsilon = 0.7$  in equation (26), these exchange rates would imply an average bubble diameter  $d \sim 0.2\text{--}0.6$  mm in a sill 2.5 km long and  $d \sim 1\text{--}3$  mm in an equant reservoir.

These values are in the bubble size range measured in lapilli from Stromboli (Lautze and Houghton, 2005) and are within the range of acceptable sizes for gas segregation to occur on a time scale shorter than the magma residence time.

We would expect normal, episodic Strombolian degassing for a magma supply rate smaller than the exchange rate, and more violent eruptions at higher supply rates. Using our model with bubble sizes consistent with gas segregation in the Stromboli shallow reservoir, we expect the transition between these two eruptive regimes to occur at a supply rate on the order of  $0.1\text{--}1 \text{ m}^3 \text{ s}^{-1}$  (Fig. 13). Landi et al. (2004) estimated the eruption rate of gas-rich material during violent recent eruptions at Stromboli at  $\sim 30 \text{ m}^3 \text{ s}^{-1}$ , implying that  $Q_s$  exceeded  $Q_{ex}$  by two orders of magnitude, in accord with our model principles.

Although our experimental work was not expressly designed to study degassing and generation of gas-poor and gas-rich magmas at a specific volcano, we have shown that the general physical principles governing gas segregation in shallow horizontal intrusions can be applied to Stromboli volcano. Model implications, in terms of the bubble sizes of exsolved gas in the shallow chamber, the fluxes of gas-poor and gas-rich magmas generated by gas segregation as well as the different eruptive regimes determined by the relative values of supply rate and exchange flow, are all consistent with a variety of independent field data.

#### *4.4 Limitations of our analysis*

Two processes that have not been accounted for in our analysis are bubble convection and thermal convection. Bubble convection effects arise as the concentration of bubbles increases. Although it is difficult to predict the onset of bubbly convection in shallow magmatic systems, and consequently laminar bubble rise is considered to be a reasonable regime, we now consider the convective regime for completeness.

Bubbly convection occurs in suspensions of uniformly-distributed bubbles when the characteristic gas bubble size  $d$  is large enough that three-dimensional inertial effects become important and bubbles are entrained in each other's wake. This is thought to occur when  $d > 4\sqrt{\sigma/(\rho_l g)}$  (Wallis, 1969), where  $\sigma$  is the coefficient of surface tension between gas and liquid, of density  $\rho_l$ . For most magmas,  $\sigma = 0.3 - 0.4 \text{ kg/s}^2$  (e.g., Williams and McBirney, 1979), and three-dimensional inertial effects are expected to be important for centimetric gas bubbles, or larger, but not for bubbles of smaller size. However, the departure from a uniform bubbly pattern can also occur due to the characteristics of the production of the gas bubbles and their interaction with the overall flow dynamics (Wallis, 1969). This effect is difficult to assess, but the associated convective velocity scale has been observed experimentally to be typically greater than laminar rise speed (e.g., Cardoso and Woods, 1999; Phillips and Woods, 2001). We note, however, that both the bubble time scale,  $T_b$ , and the foam time scale,  $T_f$ , are inversely proportional to bubble rise speed (see section 4.1). As convecting gas bubbles are expected to rise faster than in the



laminar regime, both time scales will thus decrease by the same amount. Therefore, steady-state gas segregation will be established more rapidly. This also implies that the range of magma viscosity over which gas segregation could occur is increased (see Figs. 10 and 11). Regardless of the time needed for gas segregation to occur, the same physical principles apply whether bubbles rise in a laminar or turbulent suspension, with laminar analysis leading to conservative modeling of the bubble rise and therefore of the time needed to establish steady-state gas segregation.

In deriving the cooling and solidification time scale (25), we assumed that a horizontal sill cools down by conduction. However, the impact of thermal convection in the sill also needs to be considered. Conditions for thermal convection in a sill are reached when the Rayleigh number,  $Ra$ , exceeds approximately 2000 (Sparks et al., 1984). The Rayleigh number is defined by

$$Ra = \frac{\beta \rho_l g \Delta T D^3}{\mu_l \kappa}, \quad (30)$$

where  $\beta$  is the volumetric coefficient of thermal expansion of the magma ( $2 \times 10^{-5} \text{ K}^{-1}$ ; Annen et al., 2005) and  $\Delta T$  is the temperature difference between the magma and the surrounding rocks. Application of equation (30) with a magma viscosity of  $10^5 \text{ Pa s}$  and a temperature difference of  $1^\circ \text{C}$  shows that the Rayleigh number exceeds 2000 for any sill thicker than 6 m. This indicates that thermal convection can be attained in relatively thin sills even with relatively small thermal gradients across the magma layer, as recognised in previous studies (e.g., Sparks et al., 1984; Annen et al., 2005). However, magma cooling and crystallisation induce exsolution of gas bubbles, which decreases the density and increases the viscosity of the magma. Cardoso and Woods (1999) have calculated the evolution of the Rayleigh number as the melt cools and becomes volatile saturated. Their study shows that the magnitude of the Rayleigh number, and thus the intensity of the convection, increases by a factor of 10-100 as a result of the bubble production. Convection in a horizontal intrusion will therefore be driven predominantly by the motion of gas bubbles. As shown above, we expect steady-state gas segregation to be established more rapidly than in the purely conductive case. We stress again that regardless of the time needed for gas segregation to occur, whether bubble suspension is laminar or turbulent, the same

physical principles for gas segregation apply, as captured by the present laminar analysis.

## **5. Conclusion**

Gas segregation in plumbing systems of persistent volcanoes has been investigated by means of analogue experiments in the specific case of low exsolved volumetric gas concentrations in a vertical conduit connected to a single horizontal intrusion. These experiments show that the presence of horizontal intrusions can lead to strong gas segregation effects in volcanic plumbing systems.

Gas segregation is driven by an exchange flow between the conduit and the horizontal intrusion because of the presence of exsolved bubbles. Bubbles rise and accumulate as a foam at the top of the intrusion, thereby segregating bubbles from the fluid. Bubble segregation is coupled with the accumulation of denser degassed fluid at the base of the intrusion. Steady state is ultimately reached, whereby any influx of fluid from the conduit and into the intrusion is balanced by an outward flux of lighter foam and denser degassed fluid. The length and time scales of this gas segregation are controlled by the rise of bubbles in the horizontal intrusion.

The comparison of time scales for gas segregation processes with that of the cooling and solidification of the intrusion suggests that more efficient gas segregation occurs in sills than in horizontal dikes. All time scales associated with gas segregation increase both with magma viscosity and intrusion size. However, the cooling and solidification time scale appears to be the most sensitive to intrusion size. This suggests that gas segregation could be efficient within large intrusions with magmas of basaltic to intermediate composition as well as within smaller, basaltic intrusions.

Our analysis has also implications for the generation of gas-rich and gas-poor magmas by gas segregation processes in persistent plumbing systems. For a low magma supply rate at a persistent volcano, very efficient gas segregation is expected, inducing episodic degassing and pulse-like activity that erupt relatively gas-poor magmas, because segregation rates are larger than overall magma supply rate. At higher magma supply rates, gas segregation is expected to be less

effective, leading to stronger explosions erupting gas-rich as well as gas-poor magmas.

The general physical principles governing gas segregation in shallow horizontal intrusions can be applied to Stromboli, and their implications are all consistent with independent field data. Gas segregation at Stromboli is likely to occur in a shallow reservoir of sill-like geometry at 3.5 km depth with bubbles of exsolved gas 0.1–1 mm in diameter. The transition between Strombolian activity erupting gas-poor, highly porphyritic magmas and violent explosions that erupt also gas-rich, low porphyritic magmas would correspond to a critical magma supply rate on the order of  $0.1\text{--}1\text{ m}^3\text{ s}^{-1}$ .

Our analysis of gas segregation in the conduit plumbing system was restricted to horizontal dikes and sills. The effect of more complex geometries should be addressed in future studies. Although the key physical principles that govern gas segregation are not expected to differ, the system geometry affects the extent over which gas segregation processes occur, and in turn their efficiency.

### **Acknowledgements**

This work benefitted from fruitful discussions with Brittain Hill, Steve Sparks, Andy Woods, Andrew Hogg and Gary Matson. The authors acknowledge Steve Sparks for his helpful comments and suggestions on an earlier version of this manuscript, and Brittain Hill for his thorough review of a previous version of the manuscript. This paper was prepared to document work performed by the Center for Nuclear Waste Regulatory Analyses (CNWRA) and its contractors for the U.S. Nuclear Regulatory Commission (NRC) under Contract No. NRC-02-02-012. The activities reported here were performed on behalf of the NRC Office of Nuclear Material Safety and Safeguards, Division of High Level Waste Repository Safety. This paper is an independent product of the CNWRA and does not necessarily reflect the view or regulatory position of the NRC.

## References

- Acocella, V., Neri, M., 2003. What makes flank eruptions? The 2001 Etna eruption and its possible triggering mechanisms. *Bull. Volcanol.* 65, 517–529.
- Allard, P., 1997. Endogenous magma degassing and storage at Mount Etna. *Geophys. Res. Lett.* 24, 2219–2222.
- Allard, P., Carbonnelle, J., Métrich, N., Loyer, H., Zettwoog, P., 1994. Sulphur output and magma degassing budget of Stromboli volcano. *Nature* 368, 326–330.
- Andronico, D., Branca, S., Calvari, S., Burton, M., Caltabiano, T., Corsaro, R. A., Del Carlo, P., Garfi, G., Lodato, L., Miraglia, L., Murè, F., Neri, M., Pecora, E., Pompilio, M., Salerno, G., Spampinato, L., 2005. A multi-disciplinary study of the 2002–03 Etna eruption: insights into a complex plumbing system. *Bull. Volcanol.* 67, 314–330.
- Annen, C., Scaillet, B., Sparks, R. S. J., 2005. Thermal constraints on the emplacement rate of a large intrusive complex: The Manaslu leucogranite, Nepal Himalaya. *J. Petr.*, doi:10.1093/petrology/egi068.
- Barenblatt, G. I., 1996. *Scaling, self-similarity, and intermediate asymptotics*. Cambridge University Press.
- Batchelor, G. K., 1967. *An Introduction to Fluid Dynamics*. Cambridge University Press.
- Berlo, K., Blundy, J., Turner, S., Cashman, K., Hawkesworth, C., S., B., 2004. Geochemical precursors to volcanic activity at Mount St. Helens, USA. *Science* 306, 1167–1169.
- Cardoso, S. S. S., Woods, A.W., 1996. Interfacial turbulent mixing in stratified magma reservoirs. *J. Volcanol. Geotherm. Res.* 73, 157–175.
- Cardoso, S. S. S., Woods, A. W., 1999. On convection in a volatile-saturated magma. *Earth Planet. Sci. Lett.* 168, 301–310.
- Cashman, K. V., Mangan, M. T., 1994. Physical aspects of magma degassing II. Constraints on vesiculation processes from textural studies of eruptive products. *Mineralogical Society of America, Reviews in Mineralogy* 30, 447–478.
- Chouet, B., Dawson, P., Ohminato, T., Martini, M., Saccorotti, G., Giudicepietro, F., De Luca, G., Milana, G., Scarpa, R., 2003. Source mechanisms of explosions at Stromboli Volcano, Italy, determined from moment-tensor inversions of very-long-period data. *J. Geophys. Res.* 108 (B3) (2019), doi:10.1029/2002JB001919.

- Chouet, B., Saccorotti, G., Martini, M., Dawson, P., De Luca, G., Milana, G., Scarpa, R., 1997. Source and path effects in the wave fields of tremor and explosions at Stromboli Volcano, Italy. *J. Geophys. Res.* 102, 15,129–15,150.
- Dawson, P., Whilldin, D., Chouet, B., 2004. Application of near real-time radial semblance to locate the shallow magmatic conduit at Kilauea Volcano, Hawaii. *Geophys. Res. Lett.* 31, L21606, doi:10.1029/2004GL021163.
- Francalanci, L., Tommasini, S., Conticelli, S., 2004. The volcanic activity of Stromboli in the 1906–1998 AD period: mineralogical, geochemical and isotope data relevant to the understanding of the plumbing system. *J. Volcanol. Geotherm. Res.* 131, 179–211.
- Francalanci, L., Tommasini, S., Conticelli, S., Davies, G. R., 1999. Sr isotope evidence for short magma residence time for the 20th century activity at Stromboli volcano, Italy. *Earth Planet. Sci. Lett.* 167, 61–69.
- Francis, P., Oppenheimer, C., Stevenson, D., 1993. Endogenous growth of persistent active volcanoes. *Nature* 366, 554–557.
- Giberti, G., Jaupart, C., Sartoris, G., 1992. Steady-state operation of Stromboli volcano, Italy: constraints on the feeding system. *Bull. Volcanol.* 54, 535–541.
- Harris, A. J. L., Stevenson, D. S., 1997. Magma budgets and steady-state activity of Vulcano and Stromboli. *Geophys. Res. Lett.* 24, 1043–1046.
- Huppert, H. E., 1982. The propagation of two-dimensional and axisymmetric viscous gravity currents over a rigid horizontal surface. *J. Fluid Mech.* 121, 43–58.
- Jaupart, C., Vergnolle, S., 1989. The generation and collapse of a foam layer at the roof of a basaltic magma chamber. *J. Fluid Mech.* 203, 347–380.
- Kyle, P. R., Meeker, K., Finnegan, D., 1990. Emission rates of sulfur dioxide, trace gases and metals from Mount Erebus, Antarctica. *Geophys. Res. Lett.* 17, 2125–2128.
- Landi, P., Métrich, N., Bertagnini, A., Rosi, M., 2004. Dynamics of magma mixing and degassing recorded in plagioclase at Stromboli (Aeolian Archipelago, Italy). *Contrib. Mineral. Petrol.* 147, 213–227.
- Lautze, N. C., Houghton, B. F., 2005. Physical mingling of magma and complex eruption dynamics in the shallow conduit at Stromboli volcano, Italy. *Geology* 33, 425–428.
- Le Guern, F., 1987. Mechanism of energy transfer in the lava lake of Niragongo (Zaire),

- 1959–1977. *J. Volcanol. Geotherm. Res.* 31, 17–31.
- Le Guern, F., Carbonnelle, J., Tazieff, H., 1979. Erta’Ale lava lake: heat and gas transfer to the atmosphere. *J. Volcanol. Geotherm. Res.* 6, 27–48.
- Métrich, N., Bertagnini, A., Landi, P., Rosi, M., 2001. Crystallization driven by decompression and water loss at Stromboli volcano (Aeolian Islands, Italy). *J. Petrol.* 42, 1471–1490.
- Phillips, J. C., Woods, A. W., 2001. Bubble plumes generated during recharge of basaltic magma reservoirs. *Earth Planet. Sci. Lett.* 186, 297–309.
- Phillips, J. C., Woods, A. W., 2002. Suppression of large-scale magma mixing by melt-volatile separation. *Earth Planet. Sci. Lett.* 204, 47–60.
- Ripepe, M., Ciliberto, S., Della Schiava, M., 2001. Time constraints for modeling source dynamics of volcanic explosions at Stromboli. *J. Geophys. Res.* 106, 8713–8727.
- Ryan, M. P., 1988. The mechanics and three-dimensional internal structure of active magmatic systems: Kilauea Volcano, Hawaii. *J. Geophys. Res.* 93 (B5), 4213–4248.
- Ryan, M. P., Koyanagi, R. Y., Fiske, R. S., 1981. Modeling the three-dimensional structure of macroscopic magma transport systems: application to Kilauea volcano, Hawaii. *J. Geophys. Res.* 86, 7111–7129.
- Sarda, P., Graham, D., 1990. Mid-ocean ridge popping rocks: implications for degassing at ridge crests. *Earth Planet. Sci. Lett.* 97, 268–289.
- Sisson, T. W., Layne, G. D., 1993. H<sub>2</sub>O in basalt and basaltic andesite glass inclusions from four subduction-related volcanoes. *Earth Planet. Sci. Lett.* 117, 619–635.
- Sparks, R. S. J., 2003. Dynamics of magma degassing. In: Oppenheimer, C., Pyle, D. M., Barclay, J. (Eds.), *Volcanic Degassing*. No. 213 in *Geol. Soc. London Spec. Publ.* pp. 5–22.
- Sparks, R. S. J., Barclay, J., Jaupart, C., Mader, H. M., Phillips, J. C., 1994. Physical aspects of magma degassing I. Experimental and theoretical constraints on vesiculation. *Mineralogical Society of America, Reviews in Mineralogy* 30, 413–445.
- Sparks, R. S. J., Huppert, H. E., Turner, J. S., 1984. The fluid dynamics of evolving magma chambers. *Phil. Trans. R. Soc. Lond. A* 310, 511–534.
- Stevenson, D. S., Blake, S., 1998. Modelling the dynamics and thermodynamics of volcanic degassing. *Bull. Volcanol.* 60, 307–317.
- Stoiber, R. E., Williams, S. N., Huebert, B. J., 1986. Sulfur and halogen gases at Masaya Caldera

- Comlex, Nicaragua: Total flux and variations with time. *J. Geophys. Res.* 91 (B12), 12,215–12,231.
- Turcotte, D. L., Schubert, G., 1982. *Geodynamics. Applications of Continuum Physics to Geological Problems.* John Wiley & Sons, New York.
- Vaggelli, G., Francalanci, L., Ruggieri, G., Testi, S., 2003. Persistent polybaric rests of calc-alkaline magmas at Stromboli volcano, Italy: pressure data from fluid inclusions in restitic quartzite nodules. *Bull. Volcanol.* 65, 385–404.
- Vergnolle, S., Jaupart, C., 1990. Dynamics of degassing at Kilauea Volcano, Hawaii. *J. Geophys. Res.* 95, 2793–2809.
- Wallace, P. G., 2001. Volcanic SO<sub>2</sub> emissions and the abundance and distribution of exsolved gas in magma bodies. *J. Volcanol. Geotherm. Res.* 108, 85–106.
- Wallis, G. B., 1969. *One-dimensional Two-phase Flow.* McGraw-Hill Book Company.
- Williams, H., McBirney, A. R., 1979. *Volcanology.* Freeman Cooper, San Francisco.
- Woods, A. W., Cardoso, S. S. S., 1997. Triggering basaltic volcanic eruptions by bubble-melt separation. *Nature* 385, 518–520.

Table 1

Properties of golden syrup (GS), water and sodium chloride (NaCl) mixtures.

GS:water:NaCl (mass ratio)	$\rho_l$ (kg m <sup>-3</sup> )	$\mu_l$ (mPa s)
30:60:10	1187.6 ± 0.4	3.4 ± 0.1
45:45:10	1257.6 ± 0.4	11 ± 1
60:30:10	1325.9 ± 0.4	43 ± 3



Fig. 1. Schematic diagram of the apparatus.

Fig. 2. Gas production rate  $Q_g$  as a function of electric current intensity  $I$ . The uncertainty on the measurements is represented by the symbol size. The black line represents the linear regression  $Q_g = (1.43 \pm 0.03) \times 10^{-7} \times I \text{ m}^3 \text{ s}^{-1}$  ( $R^2 = 0.99914$ ).

Fig. 3. Establishment of a steady-state exchange flow (golden syrup:water:NaCl mixture ratio is 60:30:10, no fluid flow,  $Q_g = 2.9 \times 10^{-8} \text{ m}^3 \text{ s}^{-1}$ ). Black rectangles on ruler are 1 cm high and 5 mm wide. Arrows indicate flow directions. (A) time = 4 min; the bubble rich mixture can clearly be seen as the opaque fluid in the vertical tube and the initial part of the side arm, and the black curve indicates the position of the interface between bubbly and bubble-free liquids. (B) time = 8 min; the interface has propagated further into the side arm and a more opaque foam is visible at the upper surface of the side arm. (C) time = 46 min; a steady exchange flow is established between the vertical tube and the side arm. Dashed curves show the approximate thickness of the upper foam layer and the lower degassed liquid layer.

Fig. 4. Schematic illustration of the transient exchange flow between the vertical tube and the horizontal side arm.

Fig. 5. The experimental dimensionless current length  $L^* = L(t) / L_{\max}$  compared with the theoretical dimensionless length  $\left[ \rho_l g d^2 t / (12 \mu_l D) \right]^{\frac{1}{2}}$ . Each set of symbols corresponds to measurements from a single experiment. Range of experimental conditions:  $Q_g = 1.4 \times 10^{-8} - 7.7 \times 10^{-8} \text{ m}^3 \text{ s}^{-1}$  and  $\mu_l = 7 - 40 \text{ mPa s}$ .

Fig. 6. Schematic illustration of the flow of foam.

Fig. 7. Illustration showing how the theoretical foam height was corrected. For a given foam flux, hence area perpendicular to the flow, the two-dimensional analysis underestimates the foam

height (dotted rectangle); for the same foam flux, the cap-like foam is in fact thicker because of its shape (striped area). The theoretical height was increased such that both dotted rectangle and stripped cap have identical areas, ensuring identical foam flux in both model and experiment.

Fig. 8. Variation of the steady-state foam height along the side arm in three different experiments with a 45:45:10 golden syrup:water:NaCl mixture ratio and no fluid flow. (A) Electric current intensity  $I = 0.1$  A, (B)  $I = 0.2$  A, (C)  $I = 0.3$  A. The solid line shows the prediction of the theoretical model for a foam gas fraction  $\varepsilon = 0.7$  and a bubbly gas fraction  $c = 0.7 \times I$ . The dashed line shows the prediction for a foam gas fraction  $\varepsilon = 0.9$  and a bubbly gas fraction  $c = 0.2 \times I$ .

Fig. 9. Foam heights for three different experiments with a 60:30:10 golden syrup:water:NaCl mixture ratio. Each symbol corresponds to a fluid flux in the vertical conduit: triangles, no fluid flux; diamonds,  $Q_l = 9Q_g$ ; squares,  $Q_l = 79Q_g$ .  $Q_g$  is the same in all experiments. The solid line shows the model prediction with a gas fraction  $c = 0.06$  in the bubbly layer and a gas fraction  $\varepsilon = 0.8$  in the foam.

Fig. 10. The different time scales as a function of magma viscosity for different sill sizes. (A) sill thickness  $D = 10$  m and length  $L = 1$  km (B)  $D = 100$  m and length  $L = 10$  km. The horizontal solid curve represents the solidification time  $T_s$ , the slanted solid curve represents the bubble rise time  $T_b$ , and the dashed curves represent the foam time  $T_f$  for different volumetric gas fractions: short dashes,  $c = 0.01$ ; medium dashes,  $c = 0.05$ ; long dashes,  $c = 0.1$ . Magma density  $\rho_l = 2700 \text{ kg m}^{-3}$  and gas bubbles are 1 mm in diameter for all calculations. Thick black ticks on time axis represent 1 day ( $\sim 9 \times 10^3$  s) and 1 year ( $\sim 3 \times 10^7$  s).

Fig. 11. The different time scales as a function of magma viscosity and bubble diameter  $d$  for a sill 25 m thick and 2.5 km long. The horizontal solid curve represents the solidification time  $T_s$ , the slanted thick curves represent the bubble rise time  $T_b$ , and the slanted thin curves represent the foam time  $T_f$  for different bubble diameters: short dashes,  $d = 0.1$  mm; long dashes,  $d = 1$  mm; solid curves,  $d = 10$  mm. Volumetric gas fraction  $c = 0.1$  in all calculations. Thick black ticks on time axis represent 1 day ( $\sim 9 \times 10^3$  s) and 1 year ( $\sim 3 \times 10^7$  s).

Fig. 12. Schematic illustration of an exchange flow of bubbly and degassed magma driven by steady-state gas segregation. In a system with supply rate  $Q_s$ , an exchange rate  $Q_{ex}$  of bubbly fluid entering the intrusion is balanced by an exsolved gas return rate  $Q_g$  and a degassed magma return rate  $Q_D$ :  $Q_{ex} = Q_g + Q_D$ .

Fig. 13. Exchange flow rate  $Q_{ex}$  (solid curves), exsolved gas return rate  $Q_g$  (short dashed curves) and degassed magma return rate  $Q_D$  (long dashed curves) as a function of magma viscosity. Thick lines corresponds to an average bubble diameter  $d = 1$  mm, thin lines to a diameter  $d = 0.1$  mm. We assume an intrusion 2.5 km long and wide, and a volumetric gas fraction  $c = 0.1$ .

Fig. 14. The different time scales as a function of magma viscosity for an equant reservoir 500 m in diameter. The horizontal solid curve represents the solidification time  $T_s$ , the slanted thick curves represent the bubble rise time  $T_b$ , and the slanted thin curves represent the foam time  $T_f$  for different bubble diameters: short dashes,  $d = 0.1$  mm; long dashes,  $d = 1$  mm. Volumetric gas fraction  $c = 0.1$ . Thick black ticks on time axis represent 1 day ( $\sim 9 \times 10^3$  s) and 1 year ( $\sim 3 \times 10^7$  s).

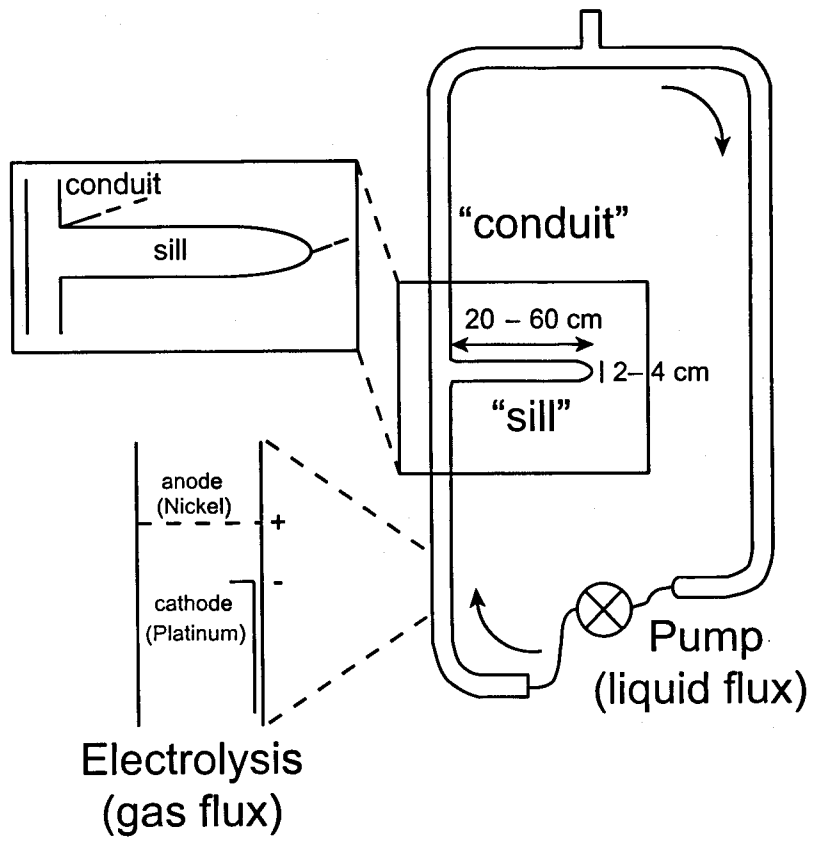


Fig. 1

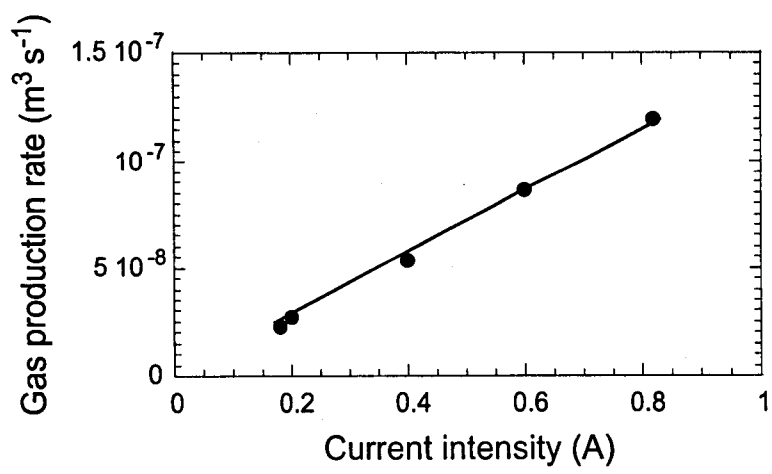


Fig. 2

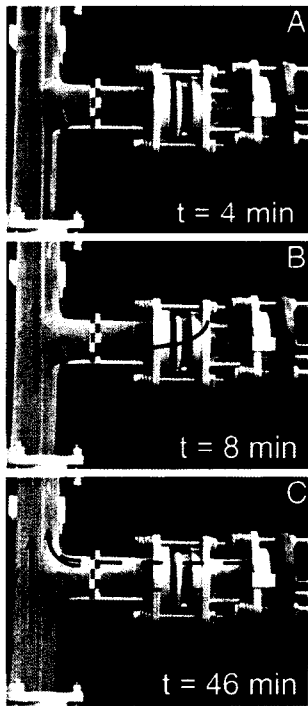


Fig. 3

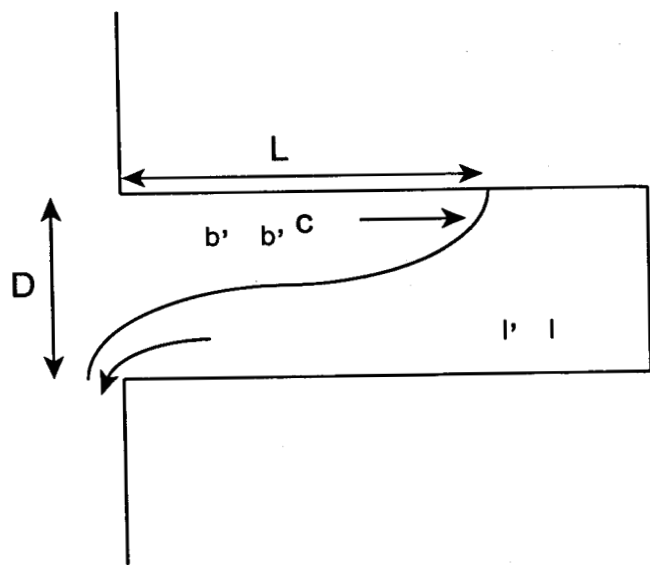


Fig. 4

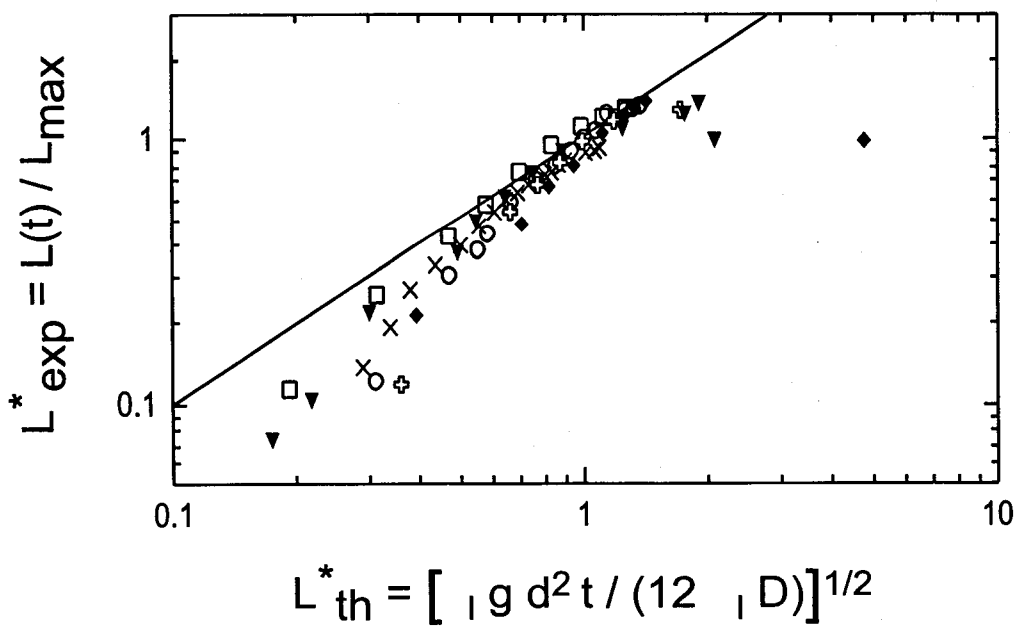


Fig. 5



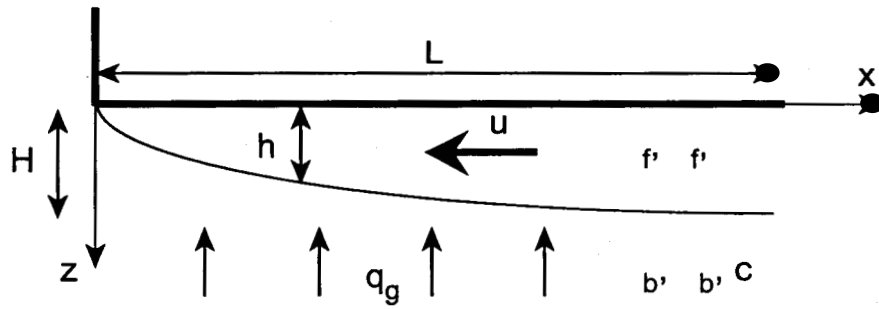


Fig. 6

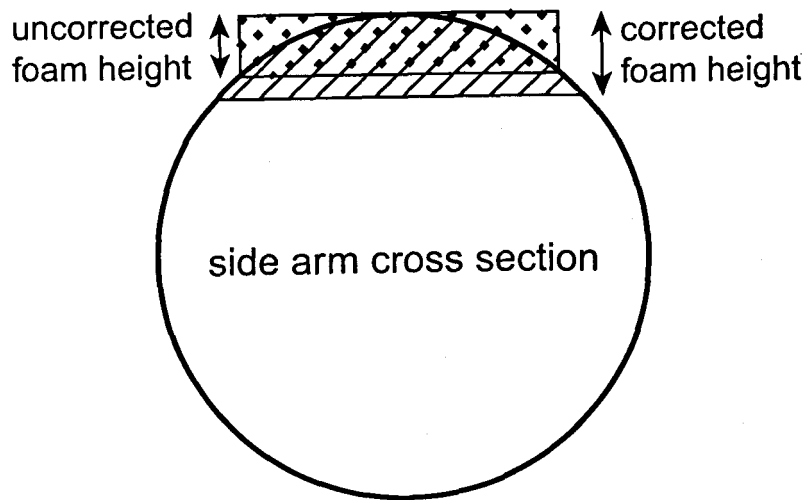


Fig. 7

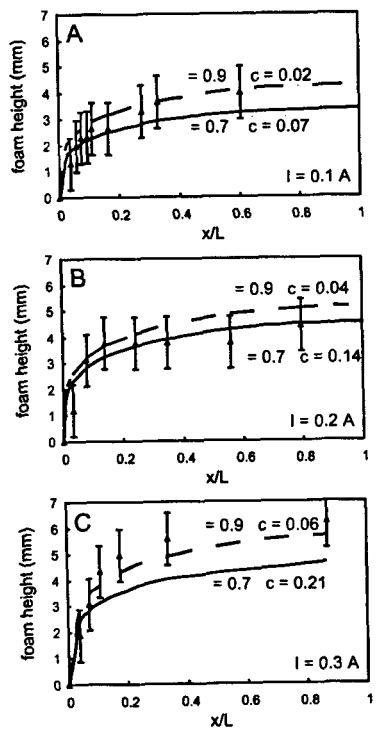


Fig. 8

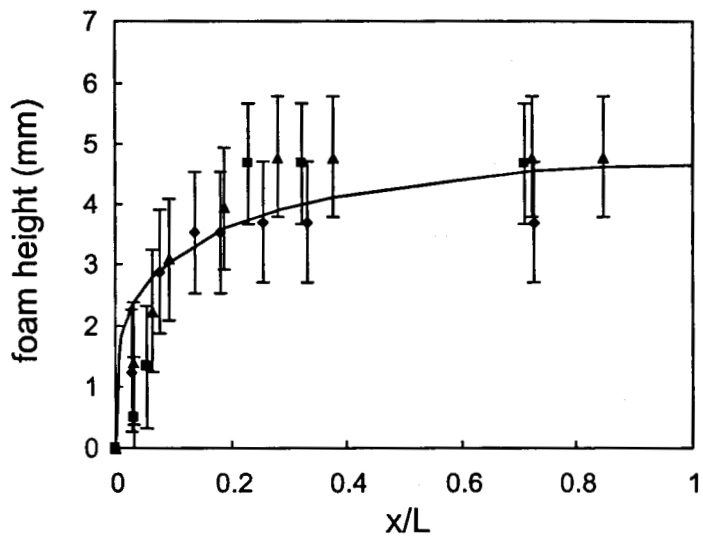


Fig. 9

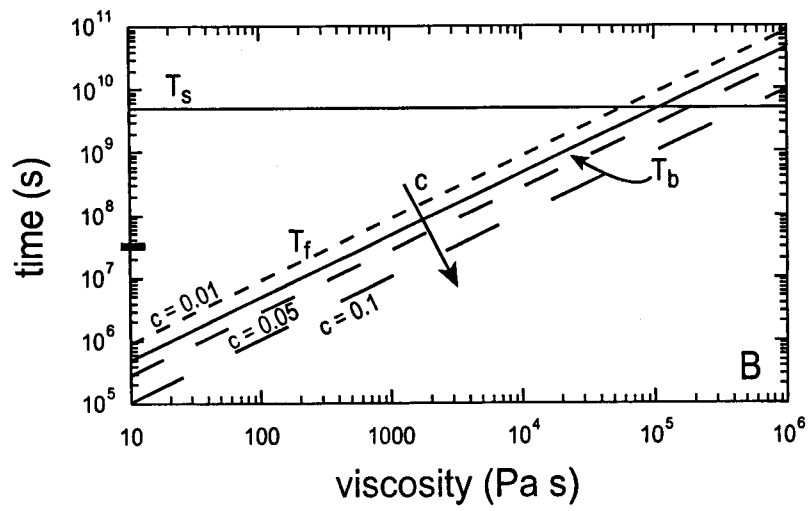
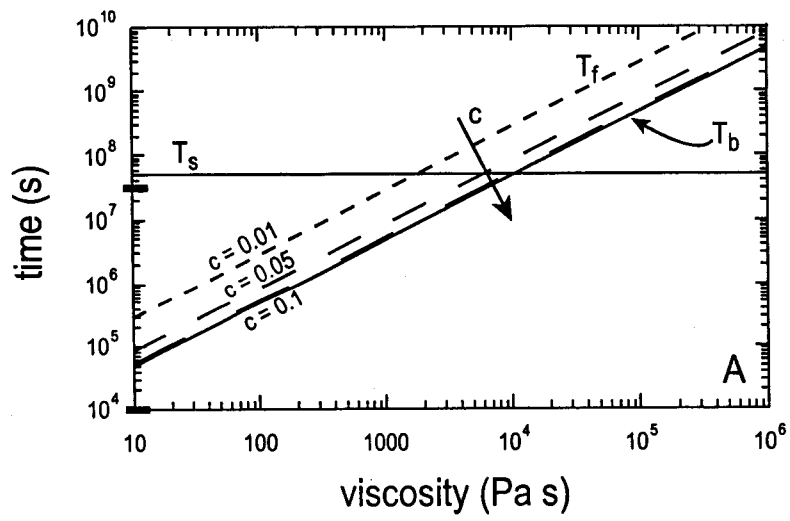


Fig. 10

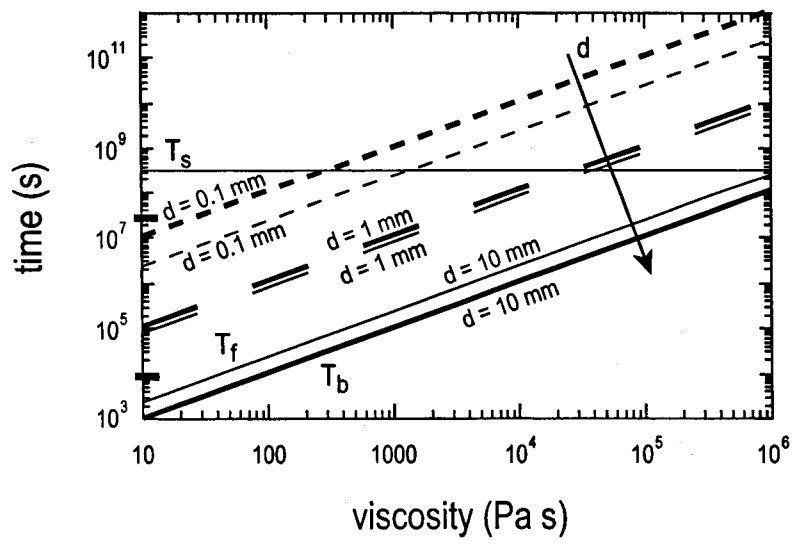


Fig. 11

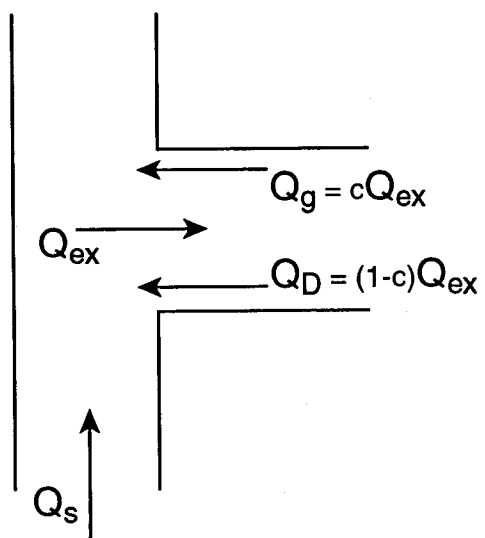


Fig.12

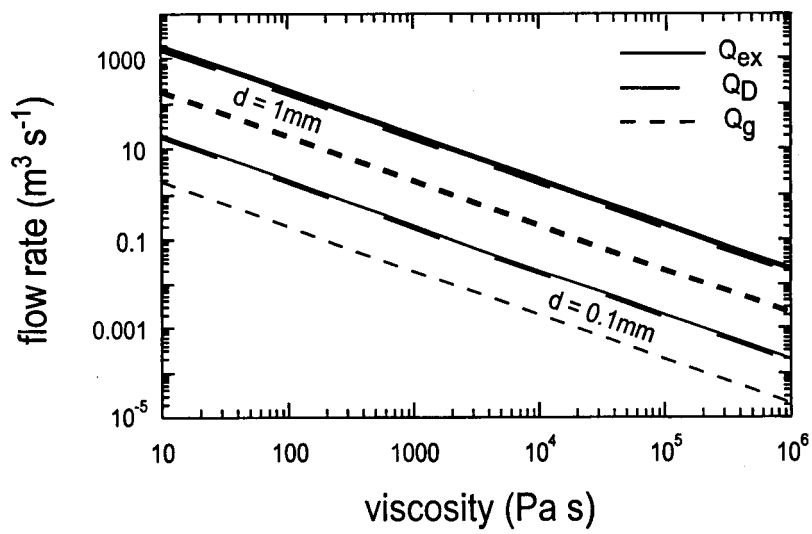


Fig. 13



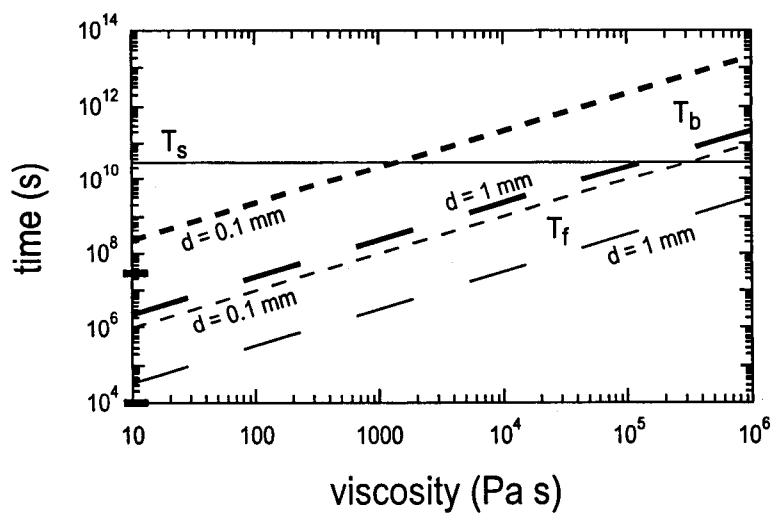


Fig. 14